Journal of Colloid and Interface Science 579 (2020) 786–793

Contents lists available at ScienceDirect

Journal of Colloid and Interface Science

journal homepage: www.elsevier.com/locate/jcis

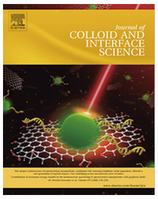

Mechanical reinforcement of polymer colloidal crystals by supercritical fluids

Visnja Babacic[a], Jeena Varghese[a], Emerson Coy[b], Eunsoo Kang[c], Mikolaj Pochylski[a], Jacek Gapinski[a], George Fytas[c], Bartlomiej Graczykowski[a,c,*]

[a] *Faculty of Physics, Adam Mickiewicz University, Uniwersytetu Poznanskiego 2, 61-614 Poznan, Poland*
[b] *NanoBioMedical Centre, Adam Mickiewicz University, Wszechnicy Piastowskiej 3, 61-614 Poznan, Poland*
[c] *Max Planck Institute for Polymer Research, Ackermannweg 10, 55128 Mainz, Germany*

GRAPHICAL ABSTRACT

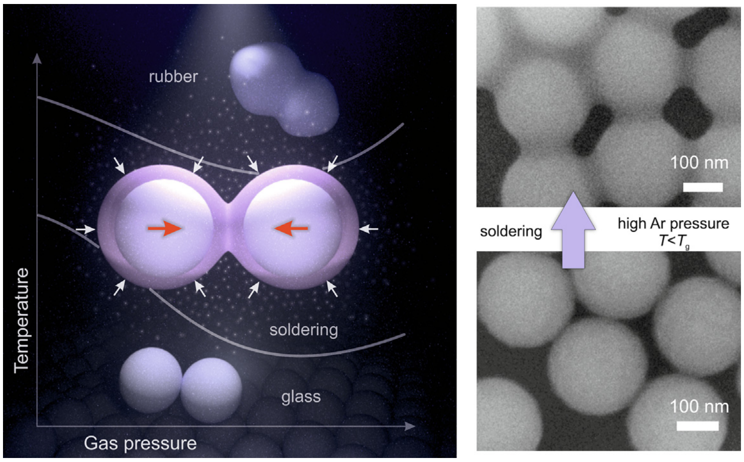

ARTICLE INFO

Article history:
Received 22 May 2020
Revised 19 June 2020
Accepted 24 June 2020
Available online 29 June 2020

Keywords:
Colloidal crystals
Plasticization
Brillouin light scattering
Phononic crystals
Photonic crystals

ABSTRACT

Colloidal crystals realized by self-assembled polymer nanoparticles have prominent attraction as a platform for various applications from assembling photonic and phononic crystals, acoustic metamaterials to coating applications. However, the fragility of these systems limits their application horizon. In this work the uniform mechanical reinforcement and tunability of 3D polystyrene colloidal crystals by means of cold soldering are reported. This structural strengthening is achieved by high pressure gas (N_2 or Ar) plasticization at temperatures well below the glass transition. Brillouin light scattering is employed to monitor in-situ the mechanical vibrations of the crystal and thereby determine preferential pressure, temperature and time ranges for soldering, *i.e.* formation of physical bonding among the nanoparticles while maintaining the shape and translational order. This low-cost method is potentially useful for fabrication and tuning of durable devices including applications in photonics, phononics, acoustic metamaterials, optomechanics, surface coatings and nanolithography.

---

* Corresponding author.
E-mail address: graczykowski@mpip-mainz.mpg.de (B. Graczykowski).

https://doi.org/10.1016/j.jcis.2020.06.104
0021-9797/© 2020 The Authors. Published by Elsevier Inc.

1. Introduction

Colloidal crystals (CCs) made of nanoparticles (NPs) are low cost volumetric materials that can exhibit unique properties enabled at nanoscale [1–3]. Because of their periodic structure, that can control the propagation of light and sound, CCs function as photonic and phononic materials [4–9]. Owing to the broad variety of polymeric materials polymer-based CCs are of interest, especially for coatings and nanolithography [10,11]. For such applications the cost effectiveness, superhydrophobicity and easy tunability of NPs size and shape is advantageous [3,12–16]. However, since self-assembled particles are weakly bonded, fragility of polymer CCs remains a critical issue when it comes to their application [1]. Disassemble of polymer CCs results in malfunctioning of the devices and, what is of even a bigger concern, in the releasing of micro/nano contaminants into the environment [17–19]. To this day, several approaches have been developed in order to enhance NP-NP bonding and hence make robust polystyrene (PS) CCs. This involves the development of core-shell structures, nanocomposites, decoration by surfactants, plasma and chemical assisted treatments, direct UV irradiation, among the others [20–24]. Thermal treatment just below the glass transition temperature (T_g), is probably one of the most straightforward approaches. In this process, the NP-NP contact area increases due to the existence of a thin mobile layer on the NP surface, above the so-called softening temperature (T_s) [25–27]. However, this process is rather slow and therefore of low efficiency and moreover not suitable for complex thermosensitive systems.

Here, we propose a route to develop robust PS CCs by combining hydrostatic gas pressure (p) and temperature (T) much lower than T_g, as illustrated in Fig. 1 (a). Exposing polymers to the hydrostatic gas pressure can modify T_g in a nontrivial manner due to the counteracting compression and plasticization effects. Several studies have already shown the effect of nitrogen, carbon dioxide, hydrofluorocarbons and methane pressure on the T_g of bulk PS [28–30]. We use Brillouin light scattering (BLS) vibrational spectroscopy [25,31,32] of interacting NPs to measure *in-situ* change of NP-NP contact area in supercritical nitrogen or argon environment. Among the experimental approaches such as Raman spectroscopy [33] and ultrafast opto-acoustics technique [34–37] we used BLS being more suitable on the account of easy transducer-free fabrication and GHz spectral regime. In this work we studied the impact of pressure on both T_s and T_g of PS CCs clusters. We then determined the (p,T) conditions favorable for strong mechanical reinforcement of the PS CCs while maintaining their periodic structure. We termed this process *cold soldering* as it is possible well below T_g of bulk PS.

2. Materials and methods

2.1. Samples

We prepared the PS CCs samples by drop casting of an aqueous dispersion of PS NPs (PS-268, diameter d = 268 ± 7 nm) onto a glass substrate. We dried the samples in low vacuum at 293 K by using a vacuum bell jar for minimum one hour. The scanning electron microscope (SEM) imaging was performed using JEOL 8001TTLS system. SEM images of CC before and after cold soldering are shown in Fig. 1 (b) and (c), respectively [2,25].

2.2. Nanoparticles vibrational modes

For a free sphere, the frequencies of the latter modes can be calculated from the formula $f_{n,l} = A_{n,l} v_{\mathrm{t}}/d$ Here, n and l are integers indicating radial and angular dependence of sphere displacement field, v_{t} denotes transverse sound velocity and $A_{n,l}$ is the dimensionless factor weakly dependent on the Poisson's ratio [38,39]. In principle, NP-NP interactions reduce the spherical symmetry and perturb all Lamb modes in the way that they split into weakly, albeit dispersive $m = 2\ l + 1$ modes (m stands for the azimuthal number). For a free sphere, the (1,1) mode is not related to any deformation and hence it has zero frequency. When NPs assemble to form fcc clusters the NP-NP contacts enable vibrational energy transfer. As a consequence, the (1,1) mode transforms into propagating waves of non-zero frequency. More details, formulas and their deviation can be found in SI.

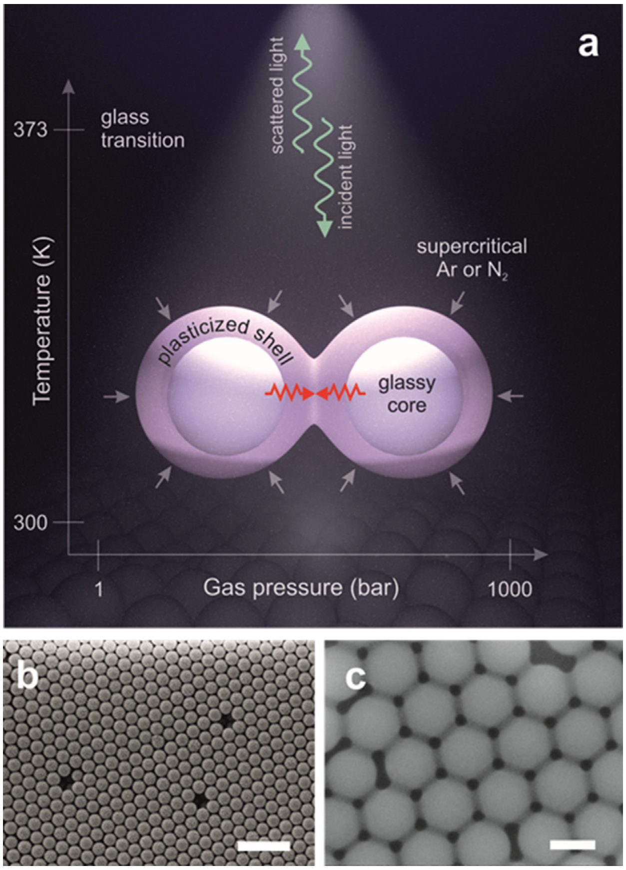

Fig. 1. (a) Schematic diagram illustrating the concept of cold soldering and the experimental approach applied for in situ monitoring of the process. At temperatures below the glass transition of PS supercritical argon or nitrogen plasticize the shell of nanoparticles. Simultaneously, hydrostatic pressure squeezes particles together increasing their contact area. The strength of the particle–particle bonding is monitored by inelastic Brillouin light scattering of GHz dipolar vibrational modes. SEM images of (b) colloidal crystals made of PS nanoparticles obtained (b) before and (c) after cold soldering. Scale bars are (b) 1 μm and (c) 200 nm.

2.3. Brillouin light scattering

We performed BLS experiment by means of high contrast tandem-type Fabry-Perot interferometer (JRS Optical Instruments) and λ = 532 nm CW laser as a source of probing light. We used the backscattering geometry with vertical and horizontal polarization of incident and scattered light, respectively. We used a custom made chamber with temperature control to apply N_2 or Ar gas pressure. More details about the experiment can be found in the Supporting Information (SI).

3. Results and discussion

Fig. 2 (left panels) displays normalized BLS spectra obtained for PS CCs exposed to different conditions, *i.e.* temperature T, gas hydrostatic pressure p and gas type (N_2 or Ar). The corresponding SEM images, obtained for spin coated samples are presented in Fig. 2 (e–h). The normalized BLS spectrum in Fig. 2 (a) recorded at ambient conditions in air (T = 300 K and p = 1 bar) reveals two broad asymmetric peaks [25,31,38]. These can be attributed to dipolar (1,1) and quadrupolar (1,2) spheroidal Lamb modes. The low frequency peak of the dipolar mode is related to NPs interactions and fitted using Asym2Sig function. Its spectral position at $f_{1,1}$ reflects the effective stiffness of the NP-NP contact $K_{\text{eff}} \propto M f_{1,1}^2$, where M is the mass of NP. Approximating these contacts by circular interfaces and assuming constant NPs mass and Young modulus the interface radius $a_0 \propto K_{\text{eff}} \propto f_{1,1}^2$ strongly impacts the frequency of the (1,1) mode (see SI) [38]. In the discussion we will focus on the (1,1) mode as its spectral position enables direct *in-situ* sensing of the NP-NP physical bonding tuned by both hydrostatic pressure and temperature treatments. The (1,2) quadrupolar mode, here represented by two Gaussian line shapes due to NP-NP interactions, is an additional indicator confirming uniform size and shape of NPs.

Self-assembled CCs at ambient condition are stable, although fragile structures of NPs bonded by weak van der Waals forces [1,2]. To calculate the expected radius a_0^{JKR} as well as experimental a_0 of NP-NP contacts from the BLS data (see SI) we use Johnson-Kendall-Roberts model (JKR) [40,41]. For the as-fabricated sample, JKR model predicts the NP-NP contact radius to be $a_0^{\text{JKR}} \cong 12$ nm. On the other hand, $f_{1,1}$ from BLS experiment at these conditions, yields $a_0 \cong 49$ nm, which is close to the value estimated from the corresponding SEM image shown in Fig. 2 (e) (about 40 nm). The higher contact radius, compared to the one predicted by JKR model, points to additional physical bonding due to fabrication impurities accumulated at the NP-NP contacts upon drying [42,43]. We note that the validity of the JKR model is limited to NP-NP contacts much smaller than the NP size [40].

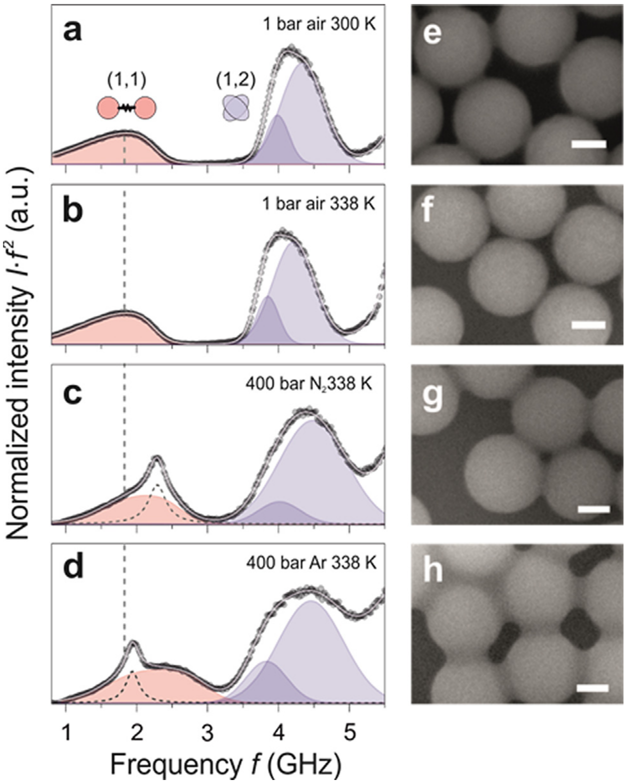

Fig. 2. Normalized BLS spectra for a cluster of PS nanoparticles (a) at ambient room conditions at 300 K, 1 bar, (b) at 338 K, 1 bar and 400 bar of hydrostatic pressure applied with either (c) N_2 or (d) Ar gas at 338 K. The interaction-induced mode (1,1) and the doublet originating in (1,2) mode are indicated by red and navy shading. The dashed vertical lines in (a-d) indicate the frequency of (1,1) mode at ambient conditions. The dashed curves in (c) and (d) stand for the Lorentzian peak fit resulting from pressure waves in N_2 and Ar, respectively. The SEM images corresponding to conditions in (a-d) are shown in (e-h), respectively. The scale bars in (e-h) are 100 nm. (For interpretation of the references to colour in this figure legend, the reader is referred to the web version of this article.)

Comparing Fig. 2 (a) with (b) we can notice that when the temperature increased to 338 K the frequency of the (1,1) mode slightly red shifts relatively to the reference spectrum at ambient conditions. This can be attributed to weak thermal softening of PS which is still in the glassy state. The NP-NP contacts are robust to this temperature increase according to the SEM image in Fig. 2 (f). However, the situation is different for the PS CC exposed to 400 bar of N_2 or Ar at 338 K as shown in Fig. 2 (c) or 2 (d). For both cases, we observe overlapping of the (1,1) mode with inelastic light scattering from the sound waves propagating in the gas [44]. This spectral contribution is represented by a Lorentz function indicated by dashed curves in Fig. 2 (c) and (d). For both gasses, $f_{1,1}$ is blue-shifted with respect to the BLS spectrum [Fig. 2 (b)] at the same T = 338 K at p = 1 bar indicating increased NP-NP contacts. However, this effect cannot be solely attributed to the compressive forces as it is gas specific and notably is more pronounced when the pressure is applied by Ar. This gas specificity is also reflected in the SEM images in Fig. 2 (g) and (h), where we notice clear NP-NP physical bonding, while NPs keep their individual spherical shape. This is further supported by the clearly resolved vibrational modes (1,2) which would be absent if a continuous PS film was formed.

To examine the effect of the gas pressure on NP-NP contacts we performed temperature-resolved BLS at fixed gas pressure. The experiments were carried out from room temperature (RT, 300 K) up over the glass transition temperature of bulk PS (373 K) with a heating rate 0.25 K/min. From Fig. 3 (a), we can infer that at ambient pressure the temperature dependence of $f_{1,1}$ reveals an inflection point at T_s. The formation of the mobile surface starts at the softening temperature T_s, as illustrated schematically in Fig. 3 (d). While self-assembled NPs exhibit weak van der Waals interactions, after reaching T_s physical bonding between NPs increases with temperature [25]. This trend can be studied up to the glass transition temperature T_g of the NPs [Fig. 3 (a)] at which the vibrational modes in the BLS spectrum vanish due to formation of a continuous PS film. Thus Fig. 3 (a) identifies $T_s = 344 \pm 3$ K and $T_g = 367 \pm 3$ K at ambient pressure. At 400 bar of N_2 or Ar the glass transition temperature T_g decreases to 360 ± 3 K or 351 ± 3 K, as shown in Fig. 3 (b) or (c). At first glance, this finding appears counterintuitive, since T_g should increase with pressure due to reduction of the polymer free volume. In particular, for bulk PS elevation of T_g by about 13 K at 400 bar can be estimated from the literature data.[45] Moreover, the reduction of T_g is stronger for Ar than for N_2. We attribute such gas-specific effect to plasticization of NPs surface due to gas permeation, which is higher in the case of Ar. Gases above their critical point are known as good solvents of polymers, increasing their free volume and changing their thermal and mechanical properties [46–48]. In principle, enhanced mobility could also occur upon expansion of polymers through dynamic yielding that speeds up the segmental dynamics [49] and T_g suppression under confinement [50,51]. The former reported and predicted [52,53] for glassy polymers should also occur for bulk PS for which, however, compression led to an elevation of T_g [45] and hence slowdown of the segmental dynamics [54]. The confinement induced decrease T_g of PS NPs is reported for diameters below about 100 nm and consequently is not observed in this study [Fig. 3(a)]. The recently reported T_g-assisted cold flow of labelled PS NPs clusters using fluorescence energy transfer technique [55] was observed upon compression

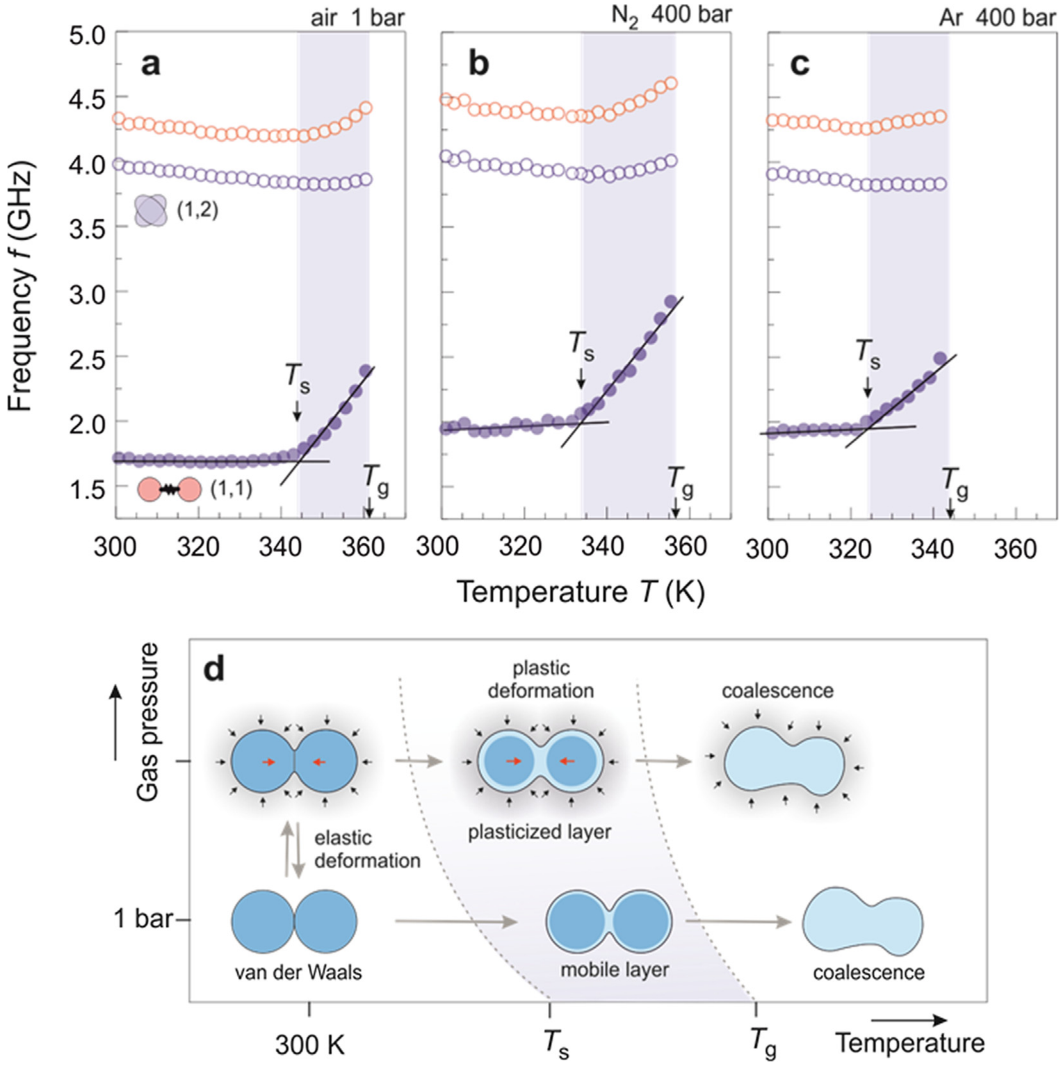

Fig. 3. Temperature dependence of the frequency of the dipolar mode (1,1) and quadrupolar mode (1,2) at (a) 1 bar (b) 400 bar of N_2 (c) 400 bar of Ar. Symbols T_g and T_s denote glass transition and softening temperatures, respectively. (d) Schematic illustration of the response of the CC to combined pressure and temperature treatment. At ambient conditions, NPs are bonded by weak van der Waals forces. At $p = 1$ bar (of air) temperature rise activates NP surface mobile layer increasing NP-NP contacts. At $p > 1$ bar (of N_2 or Ar) gas permeation increases with temperature and results in plasticized surface layer leading to strong NP-NP physical bonding. Shaded blue regions in (a-d) cover (p,T) between T_s and T_g. (For interpretation of the references to colour in this figure legend, the reader is referred to the web version of this article.)

that should slowdown the segmental dynamics. Thus, compression induced cold flow cannot be supported by our results based on unlabeled NPs using a more direct technique. The pressure induced mobility occurred at pressures lower than 400 bar and moreover exhibited gas specificity as evident from Fig. 3 (b) and (c).

We note that our approach determines a top layer $T_g(p)$ at which the periodic structure of CC is destroyed, as documented by the disappearance of the PS NP vibration spectrum at a given (p,T). Thus the reported $T_g(p)$ refers to the gas permeated shell at constant pressure and not to the core of NP that is marked with blue shaded area in the middle panel of Fig. 3 (d). For temperatures lower than T_g of polystyrene, the latter remains in the glassy state. This dynamic structure resembles core-shell NPs, *i.e.* PS-PBMA [poly(butylmethacrylate)], for which the soft PBMA shell exhibited a thickness dependent glass transition temperature lower than T_g of polystyrene [56]. Fig. 3 (d) illustrates the response of the CC to temperature and gas pressure treatment. By comparing Fig. 3 (b) and (c) with Fig. 3 (a) we conclude that when the gas pressure is applied at 300 K, $f_{1,1}$ increases to about 1.9 GHz that is independent of the gas type. This effective hardening of PS is due to the nonlinear and elastic deformation of NPs increasing the NP-NP contacts (see SI). At this initial state [left panel of Fig. 3 (b)] there is neither surface mobile layer nor plasticization, and hence the response of the material to pressure should be reversible. On the other hand, gas diffusion into NPs increases with temperature and progresses with time. Therefore the gas-induced formation of a rubbery shell as well as compressive force lead to an irreversible process of soldering, *i.e.* formation of surface plasticized PS bonding between NPs.

Fig. 3 (b) and (c) (shaded areas) indicate that soldering accelerates above the characteristic temperature T_s with the formation of a surface mobile layer. The latter enhances gas solubility compared to glassy PS surfaces. From Fig. 3 (b) and (c) we determined the softening temperature in N_2 or (Ar) at 400 bar as $T_s = 335 \pm 3$ K ($T_s = 322 \pm 3$ K). Both values are lower than the corresponding $T_s = 344 \pm 3$ K at 1 bar due to plasticization of NPs surface. As in the case of T_g, the reduction of T_s relates to the gas solubility in PS being larger for Ar than N_2.

The dependence of T_g and T_s on the pressure of N_2 or Ar, is depicted in Fig. 4 (a) and (b). This *phase diagram* (p,T) identifies the region below T_s as the polymer glassy state, whereas the region above T_g as the rubbery state and in between the region favoring soldering. In the absence of plasticization, hydrostatic pressure elevates the T_g of PS [dashed lines in Fig. 4 (a) and (b)].[45] For both gases, T_s and T_g initially decrease with pressure up to a crossover pressure. Although the diffusion of N_2 or Ar into PS and hence plasticization increases with gas pressure, the thermodynamic effect (increase of T_g with p) dominates above the crossover pressure [28]. For N_2, the crossover occurs at about 700 bar and T_g and (T_s) drops to 356 ± 3 K (320 ± 3 K). In the case of Ar environment the crossover appears at 850 bar at which T_g = 337 ± 3 K and T_s = 303 ± 3 K. Overall, the soldering phase in the case of Ar treatment appears at lower temperatures as compared to N_2 at the same pressure. Consequently, Ar is more efficient plasticizer and medium for soldering of PS CC occurring under mild conditions, *i.e.* at temperatures close to RT. As follows from Fig. 4 (a) and (b), the difference T_g - T_s > 0 is not constant but increases with p, probably due to the competing effect of pressure on T_s and T_g *via* enhanced solubility and suppressed free volume, respectively.

To complement the dynamic results with structural changes of CCs after exposure to Ar we performed SEM imaging on spin coated CC. The SEM images of Fig. 4 (c) correspond to the samples at the selected (p,T) states marked by white circles in Fig. 4 (b). At first glance, the SEM images for the samples treated in the glassy state (D and E) do not reveal any enhanced NP-NP contacts as compared to the pristine sample [Fig. 2 (e)]. On the other hand, all the remaining samples (A-C, F-I) processed under (p,T) within the soldering phase clearly show increase of NP-NP contacts. In particular, soldering is already possible at ambient pressure of air at T = 348 ± 3 K (sample A). However, it becomes much more efficient at the same temperature once assisted by Ar plasticization (sample B). Based on the images of samples B and C we conclude that Ar at moderate pressures leads to a well pronounced soldering of CC. Further increase of pressure shifts soldering to mild temperatures, as evident for samples F-I. At 700 bar (samples H and I) the pressure effect increases the packing of CC so that the sphere-like shape of NPs is lost. We note that the diagrams in Fig. 4 (a) and (b) apply to specific paths (p,T) of the treatment and depend on the rate of p and T increase due to the two involved phenomena, vitrification and gas permeation.

To quantify the efficiency and dynamics of soldering we performed time dependent BLS measurements. The samples were subjected to (p,T) conditions, the same as those marked A-I in Fig. 4 (b), by immediate heating and pressure increase (approximately 1 min.). Then, the frequency of the (1,1) mode was recorded at constant (p,T) over t = 90 min. The post-treatment measurements were performed after 12 h relaxation of the samples under ambient conditions.

Fig. 5 (a) gathers time dependence of $f_{1,1}(t)$ obtained for four samples. At 348 K and 1 bar of air $f_{1,1}(t = 0)$ is lower than the reference $f_{1,1}$ of the as-fabricated sample at RT (black arrow) due to the elastic softening of PS with the temperature jump (from 300 K to 348 K). At elevated p, the rapid surge of $f_{1,1}(t = 0)$ is due to both pressure-induced nonlinear stiffening of PS and elastic deformation increasing NP-NP contacts [Fig. 3 (d)]. The blue shift of $f_{1,1}(t)$ is well approximated by an exponential growth functions $f_{1,1}(t) = f_{1,1}(t = 0) + B\exp(-t/\tau)$, where the adjustable parameters τ and B denote the characteristic time constant and the asymptotic frequency shift, respectively. After releasing the gas pressure and cooling down to RT, we observe the drop in $f_{1,1}$, indicated by the dashed arrows in Fig. 5 (a), due to removal of the gas from PS. This finding was confirmed by transmission electron microscopy/electron energy loss spectroscopy analysis (shown in SI), which showed the similar amount of adsorbed N_2 in the treated and in the as-fabricated sample. Moreover, both N_2 and Ar are inert gases behaving as external plasticizers meaning that chemical reaction does not take place [48]. They have been used in polymer science for decades, for example as physical blowing agents for polystyrene [57]. In our experiment, by using supercritical N_2 and Ar the composition of the PS sample stays unaffected both physically and chemically. The dynamics of soldering clearly depends on (p, T) as shown from the variation of $\tau(p,T)$ in the 3D bar plot of Fig. 5 (b). At constant p, the soldering process speeds up with increasing T and is thermally activated as indicated by the Arrhenius representation [black lines in Fig. 5 (b)] of $\tau(T) = A\exp[E_a/(RT)]$. Here, E_a is the activation energy, R denotes the gas constant and A is the high temperature pre-factor. At 400 bar and 700 bar, E_a = 43 ± 2 kJ mol^{-1} and A = 2 ± 0.7 10^{-4} s. The Arrhenius activation process is clearly distinct from the strong non-Arrhenius temperature dependence of the primary glass-rubber (α-) relaxation process related to the glass transition in amorphous bulk polymers [58]. As the experiments were performed at T intermediate between T_g and T_s, this anticipated disparity suggests fast gas diffusion facilitated by the mobile surface

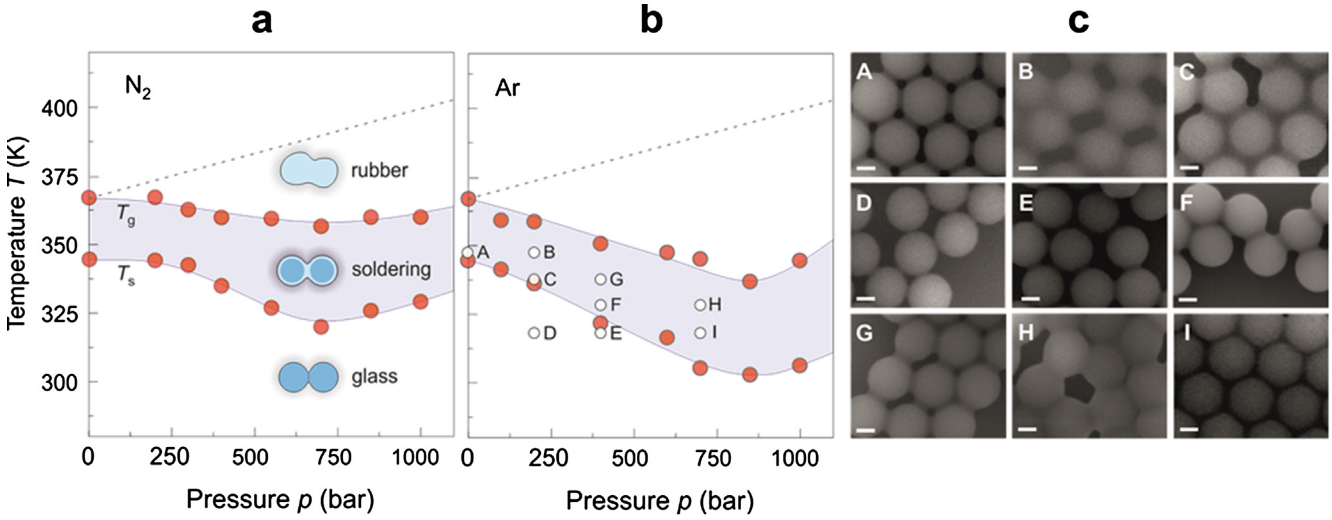

Fig. 4. Temperature-pressure phase diagram when (a) N_2 and (b) Ar pressure is applied. The glass transition T_g and the softening temperature T_s determined from BLS are shown by red solid circles, respectively. Dashed line indicates the increase of T_g with p resulting from hydrostatic pressure effect excluding plasticization. Solid lines in (a) and (b) are guides to the eye outlining the soldering region marked by the shaded area. SEM images correspond to the fixed (p,T) conditions when Ar pressure is applied, marked with white circles in Ar phase diagram. The scale bar is 100 nm. (For interpretation of the references to colour in this figure legend, the reader is referred to the web version of this article.)

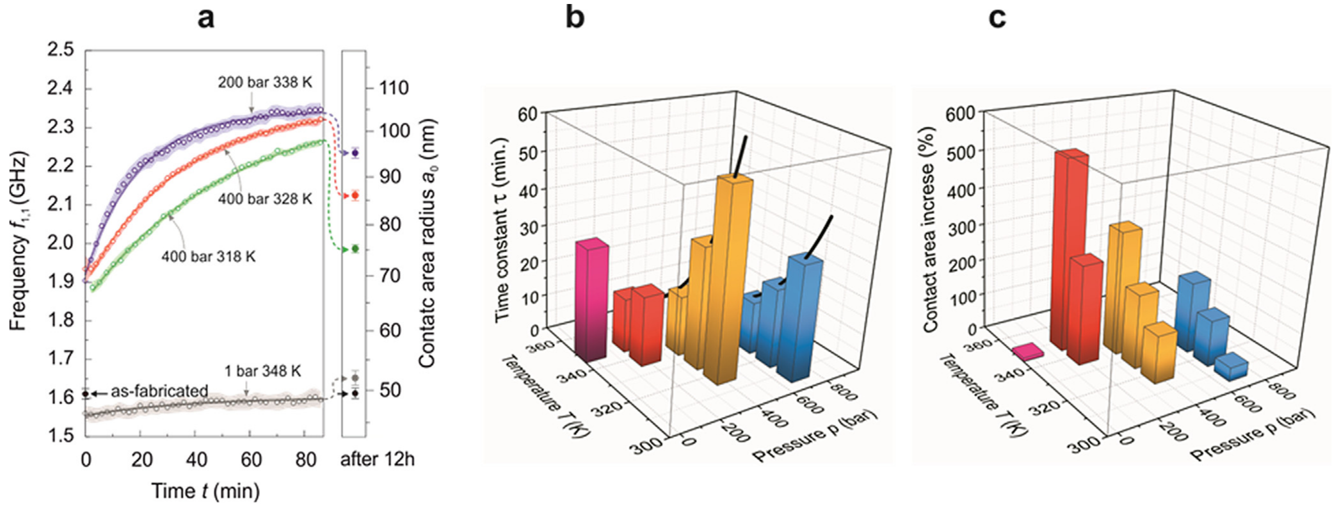

Fig. 5. (a) Time dependence of the (1,1) mode frequency at constant (p,T) conditions (open circles). Full black circle points to the $f_{1,1}$ of as-prepared sample. Right side axis stands for the calculated radius of contact area. Full circles indicated with blue, red, green and gray dashed arrows stand for $f_{1,1}$ after the corresponding treatments followed by 12 h relaxation at ambient conditions. Solid lines in indicate experimental data fits using exponential decay function. (b) Time constants τ determined from $f_{1,1}$(t) at selected conditions (p,T) in the soldering region. Solid lines denote the Arrhenius representation of τ (T) at 400 bar and 700 bar. (c) Increase of the NP-NP contact area determined for selected (p,T). (For interpretation of the references to colour in this figure legend, the reader is referred to the web version of this article.)

layer ($T > T_s$). At constant T, τ (p) increases with p [Fig. 5 (b)] due to the domination of the enhanced gas permeation over the elevation of T_g.

To quantify the effectiveness of the soldering we determine NP-NP contact area radius from $f_{1,1}$ by means of JKR model (see SI for details). The calculated a_0, plotted in the right panel in Fig. 5 (a), reveals an increase with respect to the as-fabricated sample clearly depending on the preset (p,T) conditions. In particular, treatment at p = 200 bar and T = 338 K leads to a_0 which corresponds to about 280% increase of the NP-NP contact area. For comparison, solely thermal treatment at even higher temperature T = 348 K results only in 12%. Additionally, from f_{11} we calculated the effective elastic constant $C_{11}^{\mathrm{eff}} \propto f_{11}^2$, [38,59] (described in SI) assuming there is no change in mass density of both polystyrene and fcc packed PS CC. For the as-prepared sample, $C_{11}^{\mathrm{eff}'} \approx 0.71\,\mathrm{GPa}$ and after the treatment at 338 K and 200 bar of Ar, $C_{11}^{\mathrm{eff}''} \approx 1.38\,\mathrm{GPa}$. The effective elastic constant describes the stiffness of the material. The relative change in effective elastic constant indicates nearly twice higher stiffness, which confirms the mechanical reinforcement of polystyrene by the described (p,T) treatments. Furthermore, by testing the resilience of the PS samples to mechanical impact we have demonstrated the improved robustness achieved by the supercritical gas treatment under soldering conditions (see SI for details).

It is clear that pressure assisted soldering is much more efficient in comparison to exclusively thermal treatment at ambient pressure. For selected (p,T) states, the effective change of the NP-NP contact area is displayed in Fig. 5 (c). The contact area increases with temperature and constant pressure and at a lesser extent with pressure, isothermally. Hence, the best performance appears already at moderate pressure, namely 200 bar and T = 348 K. The advantage of high pressure environment results from both plasticization of the surface and hydrostatic force increasing the NP-NP contacts. The duration of the treatment is an additional experimental parameter controlling the extent of soldering as shown by Fig. 5 (a) and (c).

4. Conclusions

We investigated the enhancement of the inter-particle bonding between PS nanoparticles at high N_2 /Ar pressure by *in-situ* BLS. The stronger physical bonding between nanoparticles was achieved by the increase in their contact area at high hydrostatic gas pressure, accompanied by plasticization effect. We showed that diffusion of gas into PS causes reduction of the glass transition temperature, T_g and the nanoparticle surface softening temperature T_s as a result of a gas specific plasticizing effect. We presented phase diagrams, for both N_2 and Ar, and identified the soldering (p, T) conditions favorable for strong physical bonding between nanoparticles, while their shape and periodicity of colloidal crystals is preserved. Soldering can occur at almost ambient temperature but at elevated gas pressures. In addition to the pressure and temperature, the duration of the treatment is an additional experimental parameter controlling the kinetics and the extent of soldering. Therefore, the gas pressure treatment provides an efficient and simple solution for the preparation of robust polymer colloidal crystalline films. Importantly, the presented results open new opportunities of application for other polymeric systems and architectures, especially to those in which temperature or other chemical processes are undesirable. Although we used N_2 and Ar, the plasticizing effect of other gases that are known to behave as solvents for polymers, such as supercritical CO_2 [60,61] or Xe, [62] can be also investigated in the near future.

Declaration of Competing Interest

The authors declare that they have no known competing financial interests or personal relationships that could have appeared to influence the work reported in this paper.

Acknowledgements

The work was supported by the Foundation for Polish Science (POIR.04.04.00-00-5D1B/18) and ERC AdG SmartPhon (Grant No. 694977). The authors thank S. Mielcarek for providing access to BLS instrumentation.

Appendix A. Supplementary data

Supplementary data to this article can be found online at https://doi.org/10.1016/j.jcis.2020.06.104.

References

[1] H. Cong, B. Yu, J. Tang, Z. Li, X. Liu, Current status and future developments in preparation and application of colloidal crystals, Chem. Soc. Rev. 42 (2013) 7774–7800.

[2] N. Vogel, M. Retsch, C.-A. Fustin, A. del Campo, U. Jonas, Advances in colloidal assembly: the design of structure and hierarchy in two and three dimensions, Chem. Rev. 115 (2015) 6265–6311, https://doi.org/10.1021/cr400081d.

[3] X. Liang, R. Dong, J.C. Ho, Self-assembly of colloidal spheres toward fabrication of hierarchical and periodic nanostructures for technological applications, Adv. Mater. Technol. 4 (2019) 1800541.

[4] M. Maldovan, E.L. Thomas, Periodic Materials and Interference Lithography: For Photonics, Phononics and Mechanics, 1 edition, Wiley-VCH, Weinheim, 2008.

[5] K. Zhong, J. Li, L. Liu, S. Van Cleuvenbergen, K. Song, K. Clays, Instantaneous, simple, and reversible revealing of invisible patterns encrypted in robust hollow sphere colloidal photonic crystals, Adv. Mater. 30 (2018) 1707246.

[6] J. Hou, M. Li, Y. Song, Recent advances in colloidal photonic crystal sensors: Materials, structures and analysis methods, Nano Today 22 (2018) 132–144, https://doi.org/10.1016/j.nantod.2018.08.008.

[7] V. Laude, Phononic Crystals: Artificial Crystals for Sonic, Acoustic, and Elastic Waves, Expanded, Revised edition, De Gruyter, Boston, 2020.

[8] J. Wang, U. Sultan, E.S.A. Goerlitzer, C.F. Mbah, M. Engel, N. Vogel, Structural color of colloidal clusters as a tool to investigate structure and dynamics, Adv. Funct. Mater. 1907730 (2019), https://doi.org/10.1002/adfm.201907730.

[9] M.A. Ghanem, A. Khanolkar, H. Zhao, N. Boechler, Nanocontact tailoring via microlensing enables giant postfabrication mesoscopic tuning in a self-assembled ultrasonic metamaterial, Adv. Funct. Mater. 30 (2020) 1909217, https://doi.org/10.1002/adfm.201909217.

[10] J. Zhang, B. Yang, Patterning colloidal crystals and nanostructure arrays by soft lithography, Adv. Funct. Mater. 20 (2010) 3411–3424, https://doi.org/10.1002/adfm.201000795.

[11] J. Semmler, K. Bley, R.N. Klupp Taylor, M. Stingl, N. Vogel, Particulate coatings with optimized haze properties, Adv. Funct. Mater. 29 (2019) 1806025, https://doi.org/10.1002/adfm.201806025.

[12] S. Jiang, A. Van Dyk, A. Maurice, J. Bohling, D. Fasano, S. Brownell, Design colloidal particle morphology and self-assembly for coating applications, Chem. Soc. Rev. 46 (2017) 3792–3807, https://doi.org/10.1039/C6CS00807K.

[13] J. Zhang, Z. Sun, B. Yang, Self-assembly of photonic crystals from polymer colloids, Curr. Opin. Colloid Interface Sci. 14 (2009) 103–114, https://doi.org/10.1016/j.cocis.2008.09.001.

[14] Z.Q. Sun, X. Chen, J.H. Zhang, Z.M. Chen, K. Zhang, X. Yan, Y.F. Wang, W.Z. Yu, B. Yang, Nonspherical colloidal crystals fabricated by the thermal pressing of colloidal crystal chips, Langmuir 21 (2005) 8987–8991, https://doi.org/10.1021/la051185w.

[15] L. Luo, E.M. Akinoglu, L. Wu, T. Dodge, X. Wang, G. Zhou, M.J. Naughton, K. Kempa, M. Giersig, Nano-bridged nanosphere lithography, Nanotechnology. 31 (2020), https://doi.org/10.1088/1361-6528/ab7c4c 245302.

[16] C. Argyo, V. Weiss, C. Brauchle, T. Bein, Multifunctional mesoporous silica nanoparticles as a universal platform for drug delivery, Chem. Mater. 26 (2014) 435–451.

[17] J. Liu, Y. Ma, D. Zhu, T. Xia, Y. Qi, Y. Yao, X. Guo, R. Ji, W. Chen, Polystyrene nanoplastics-enhanced contaminant transport: role of irreversible adsorption in glassy polymeric domain, Environ. Sci. Technol. 52 (2018) 2677–2685, https://doi.org/10.1021/acs.est.7b05211.

[18] E. Besseling, B. Wang, M. Lurling, A.A. Koelmans, Nanoplastic affects growth of S. obliquus and reproduction of D. magna, Environ. Sci. Technol. 48 (2014) 12336–12343.

[19] Y. Chae, Y.-J. An, Effects of micro- and nanoplastics on aquatic ecosystems: Current research trends and perspectives, Mar. Pollut. Bull. 124 (2017) 624–632, https://doi.org/10.1016/j.marpolbul.2017.01.070.

[20] B. You, N. Wen, L. Shi, L. Wu, J. Zi, Facile fabrication of a three-dimensional colloidal crystal film with large-area and robust mechanical properties, J. Mater. Chem. 19 (2009) 3594–3597.

[21] P. Wang, B. Sun, T. Yao, M. Chen, X. Fan, H. Han, L. Li, C. Wang, A novel dissolution and resolidification method for preparing robust superhydrophobic polystyrene/silica composite, Chem. Eng. J. 326 (2017) 1066–1073, https://doi.org/10.1016/j.cej.2017.06.058.

[22] Y. Zhang, X. Hao, J. Zhou, Y. Zhang, J. Wang, Y. Song, L. Jiang, Tough and hydrophilic photonic crystals obtained from direct UV irradiation, Macromol. Rapid Commun. 31 (2010) 2115–2120, https://doi.org/10.1002/marc.201000495.

[23] L. Wegewitz, A. Prowald, J. Meuthen, S. Dahle, O. Höfft, F. Endres, W. Maus-Friedrichs, Plasma chemical and chemical functionalization of polystyrene colloidal crystals, PCCP 16 (2014) 18261–18267.

[24] Y. Liu, B. Fan, Q. Shi, D. Dong, S. Gong, B. Zhu, R. Fu, S.H. Thang, W. Cheng, Covalent-Cross-Linked Plasmene Nanosheets, ACS Nano 13 (2019) 6760–6769.

[25] H. Kim, Y. Cang, E. Kang, B. Graczykowski, M. Secchi, M. Montagna, R.D. Priestley, E.M. Furst, G. Fytas, Direct observation of polymer surface mobility via nanoparticle vibrations, Nat. Commun. 9 (2018) 2918.

[26] R.D. Priestley, L.J. Broadbelt, J.M. Torkelson, K. Fukao, Glass transition and α-relaxation dynamics of thin films of labeled polystyrene, Phys. Rev. E 75 (2007) 061806.

[27] Z. Yang, Y. Fujii, F.K. Lee, C.-H. Lam, O.K. Tsui, Glass transition dynamics and surface layer mobility in unentangled polystyrene films, Science 328 (2010) 1676–1679.

[28] W.-C.-V. Wang, E.J. Kramer, W.H. Sachse, Effects of high-pressure CO2 on the glass transition temperature and mechanical properties of polystyrene, J. Polymer Sci. 20 (1982) 1371–1384.

[29] S.A. Boyer, J.-P.-E. Grolier, Modification of the glass transitions of polymers by high-pressure gas solubility, Pure Appl. Chem. 77 (2005) 593–603.

[30] M. Ribeiro, L. Pison, J.-P. Grolier, Modification of polystyrene glass transition by high pressure methane, Polymer 42 (2001) 1653–1661.

[31] B. Graczykowski, N. Vogel, K. Bley, H.-J. Butt, G. Fytas, Multiband hypersound filtering in two-dimensional colloidal crystals: adhesion, resonances, and periodicity, Nano Lett. 20 (2020) 1883–1889.

[32] A. Girard, J. Ramade, J. Margueritat, D. Machon, L. Saviot, F. Demoisson, A. Mermet, Contact laws between nanoparticles: the elasticity of a nanopowder, Nanoscale. 10 (2018) 2154–2161.

[33] L. Saviot, S. Le Gallet, F. Demoisson, L. David, G. Sudre, A. Girard, J. Margueritat, A. Mermet, Inelastic light scattering contribution to the study of the onset of sintering of a nanopowder, The J. Phys. Chem. C. 121 (2017) 2487–2494.

[34] J. Avice, C. Boscher, G. Vaudel, G. Brotons, V. Juve, M. Edely, C. Méthivier, V.E. Gusev, P. Belleville, H. Piombini, Controlling the nanocontact nature and the mechanical properties of a silica nanoparticle assembly, J. Phys. Chem. C. 121 (2017) 23769–23776.

[35] C.L. Poyser, T. Czerniuk, A. Akimov, B.T. Diroll, E.A. Gaulding, A.S. Salasyuk, A.J. Kent, D.R. Yakovlev, M. Bayer, C.B. Murray, Coherent acoustic phonons in colloidal semiconductor nanocrystal superlattices, ACS Nano 10 (2016) 1163–1169.

[36] A. Ayouch, X. Dieudonné, G. Vaudel, H. Piombini, K. Vallé, V. Gusev, P. Belleville, P. Ruello, Elasticity of an assembly of disordered nanoparticles interacting via either Van der Waals-bonded or covalent-bonded coating layers, ACS Nano 6 (2012) 10614–10621.

[37] J.D. Greener, E. de Lima Savi, A.V. Akimov, S. Raetz, Z. Kudrynskyi, Z.D. Kovalyuk, N. Chigarev, A. Kent, A. Patané, V. Gusev, High-Frequency Elastic Coupling at the Interface of van der Waals Nanolayers Imaged by Picosecond Ultrasonics, ACS Nano 13 (2019) 11530–11537.

[38] M. Mattarelli, M. Montagna, T. Still, D. Schneider, G. Fytas, Vibration spectroscopy of weakly interacting mesoscopic colloids, Soft Matter 8 (2012) 4235–4243.

[39] H. Lamb, On the vibrations of an elastic sphere, Proceedings of the London Mathematical Society. 1 (1881) 189–212.

[40] J.N. Israelachvili, Intermolecular and Surface Forces, Elsevier Science, 2015. https://books.google.pl/books?id=MVbWBhubrgIC.

[41] K.L. Johnson, K. Kendall, A.D. Roberts, Surface Energy and the Contact of Elastic Solids, Proc. R. Soc. A: Mathematical, Physical and Engineering Sciences. 324 (1971) 301–313, https://doi.org/10.1098/rspa.1971.0141.

[42] M. Rey, T. Yu, R. Guenther, K. Bley, N. Vogel, A dirty story: Improving colloidal monolayer formation by understanding the effect of impurities at the air/water interface, Langmuir 35 (2018) 95–103.

[43] M.A. Ghanem, A. Khanolkar, S.P. Wallen, M. Helwig, M. Hiraiwa, A.A. Maznev, N. Vogel, N. Boechler, Longitudinal eigenvibration of multilayer colloidal crystals and the effect of nanoscale contact bridges, Nanoscale. 11 (2019) 5655–5665.

[44] G. Fytas, G. Meier, T. Dorfmueller, Rayleigh-Brillouin spectra of poly [(phenylmethyl) siloxane] under high pressures, Macromolecules 18 (1985) 993–996.

[45] A. Quach, R. Simha, Pressure-volume-temperature properties and transitions of amorphous polymers; polystyrene and poly (orthomethylstyrene), J. Appl. Phys. 42 (1971) 4592–4606.

[46] S.H. Mahmood, C.L. Xin, P. Gong, J.H. Lee, G. Li, C.B. Park, Dimethyl ether's plasticizing effect on carbon dioxide solubility in polystyrene, Polymer 97 (2016) 95–103, https://doi.org/10.1016/j.polymer.2016.05.018.

[47] W.R. Vieth, P.M. Tam, A.S. Michaels, Dual sorption mechanisms in glassy polystyrene, J. Colloid Interface Sci. 22 (1966) 360–370, https://doi.org/10.1016/0021-9797(66)90016-6.

[48] E.H. Immergut, H.F. Mark, Principles of plasticization, in: ACS Publications, 1965.

[49] H.-N. Lee, K. Paeng, S.F. Swallen, M. Ediger, Direct measurement of molecular mobility in actively deformed polymer glasses, Science 323 (2009) 231–234.

[50] C. Zhang, Y. Guo, R.D. Priestley, Glass transition temperature of polymer nanoparticles under soft and hard confinement, Macromolecules 44 (2011) 4001–4006.

[51] S. Feng, Z. Li, R. Liu, B. Mai, Q. Wu, G. Liang, H. Gao, F. Zhu, Glass transition of polystyrene nanospheres under different confined environments in aqueous dispersions, Soft Matter 9 (2013) 4614–4620.

[52] R.A. Riggleman, K.S. Schweizer, J.J. de Pablo, Nonlinear creep in a polymer glass, Macromolecules 41 (2008) 4969–4977.

[53] K. Chen, K.S. Schweizer, Microscopic constitutive equation theory for the nonlinear mechanical response of polymer glasses, Macromolecules 41 (2008) 5908–5918.

[54] G. Fytas, A. Patkowski, G. Meier, T. Dorfmüller, A high pressure photon correlation study of bulk poly (methylacrylate). Comparison with relaxation processes in poly (ethylacrylate) and related polymethacrylates, J. Chem. Phys. 80 (1984) 2214–2220.

[55] X. Li, C. Zhang, Y. Sha, L. Li, D. Zhou, Z. Zhang, G. Xue, X. Wang, Cold flow of three-dimensional confined polymer systems, Polymer 111 (2017) 67–72.

[56] E. Kang, B. Graczykowski, U. Jonas, D. Christie, L.A. Gray, D. Cangialosi, R.D. Priestley, G. Fytas, Shell Architecture Strongly Influences the Glass Transition, Surface Mobility, and Elasticity of Polymer Core-Shell Nanoparticles, Macromolecules 52 (2019) 5399–5406.

[57] C. Jacob, S.K. Dey, Inert Gases as Alternative Blowing Agents for Extruded Low-Density Polystyrene Foam, J. Cell. Plast. 31 (1995) 38–47, https://doi.org/10.1177/0021955X9503100103.

[58] G. Fytas, C. Wang, G. Meier, E. Fischer, Photon correlation spectroscopic studies of poly (vinyl acetate) above the glass transition temperature, Macromolecules 18 (1985) 1492–1496.

[59] M. Levy, H.E. Bass, R.R. Stern, eds., Modern acoustical techniques for the measurement of mechanical properties, Academic Press, San Diego, 2001.

[60] F. Rindfleisch, T.P. DiNoia, M.A. McHugh, Solubility of polymers and copolymers in supercritical CO2, J. Phys. Chem. 100 (1996) 15581–15587.

[61] C.L. Bray, B. Tan, S. Higgins, A.I. Cooper, Polymer CO2 Solubility. Structure/Property Relationships in Polyester Libraries, Macromolecules 43 (2010) 9426–9433.

[62] J.H. Simpson, W.-Y. Wen, A.A. Jones, P.T. Inglefield, J.T. Bendler, Diffusion coefficients of xenon in polystyrene determined by xenon-129 NMR spectroscopy, Macromolecules 29 (1996) 2138–2142.